Fe3O4@SiO2-L-Cu(II): An efficient and easily recoverable catalyst for reducing/degrading environmental pollutants in aqueous medium

Jaber Dadashi
University of Qom
Mohammad Khaleghian
University of Qom
Babak Mir Tamizdoust (babakm.tamizdoust@gmail.com)
University of Qom

Research Article

Keywords: Copper nanocomplex, Core/shell structure, Fe3O4 nanoparticles, Environmental pollutant, Dye degradation

Posted Date: June 14th, 2021

DOI: https://doi.org/10.21203/rs.3.rs-611020/v1

Abstract

In the present study, a magnetically recoverable catalyst is synthesized through immobilizing copper (II) over the Fe_3O_4@SiO_2 nanoparticles (NPs) surface [Fe_3O_4@SiO_2-L-Cu (II)] (L = pyridine-4-carbaldehyde thiosemicarbazide). Accordingly, synthesized catalysts were determined and characterized by energy dispersive X-ray spectrometry (EDS), Fourier transforms infrared spectroscopy (FT-IR), X-ray diffraction (XRD), field emission scanning electron microscopy (FESEM), vibrating sample magnetometer (VSM), and thermogravimetric-differential thermal analysis (TG-DTA) procedures. Using [Fe_3O_4@SiO_2-L-Cu (II)], 4-Nitrophenol (4-NP), Cr(VI), and organic dyes, e.g., Methylene blue (MB) and Congo Red (CR) were reduced in aqueous media. As shown by results of Catalytic performance investigations, [Fe3O4@SiO2-L-Cu (II)] performance was outstanding concerning reduction reactions in mild conditions. Remarkable attributes of this method are high efficiency, removal of a homogeneous catalyst, easy recovery from the reaction mix, and uncomplicated route. The amount of activity in this catalytic system was almost constant after several stages of recovery and reuse. The results show that the catalyst was efficient and easily recoverable in the successive run without a significant loss of catalytic efficiency.

1. Introduction

Nitroarene compounds and toxic dyes are the main pollutants in the wastewater of various industries, including textile and dyeing industries, explosives production, cosmetics production, food industry, pharmaceutical, and paper industries[1,2]. These synthetic organic compounds are highly toxic and one of the most resistant pollutants in the environment[3]. Also, they have adverse effects on the central nervous system, liver, and blood of animals and humans. Developing an effective and simple method for the degradation of non-biodegradable pollutants into non-hazardous products is one of the serious challenges in environmental studies[4,5]. Among the various methods, chemical reduction with a reducing material is an economical and effective method for removing dyes[6]. For example, 4-aminophenol, which is the product of 4-nitrophenol reduction, is a useful and important compound[7]. This compound is widely used as the main intermediate in the pharmaceutical and dyeing industries[8]. However, the chemical reduction of dyes is a very slow process, and the use of a suitable catalyst is a serious need for the development of this method.

Among the heavy metals in industrial effluents, chromium is one of the most critical pollutants in water and wastewater, which is necessary to remove from polluted water. Improper use and discharge of effluents from these industries to the environment will pose many risks to humans and ecosystems[9]. Chromium is one of the most widely used industrial elements, mainly in the form of trivalent and hexavalent chromium in the environment[10]. Cr (VI) is highly toxic due to the formation of free radicals in cells and has been identified by many reputable international organizations as the cause of lung cancer[11]. Other side effects of Cr (VI) in the body include perforation of the septum, skin allergies, dermatitis, disorders of the stomach, liver, and kidneys[12,13]. Cr (VI) is highly soluble in water and can

form divalent anions such as chromate (CrO_4^{2-}), dichromate ($Cr_2O_7^{2-}$), and hydrogen chromate ($HCrO_4^-$) at different PHs[14,15].

To date, many various catalysts have been synthesized and used to facilitate the conversion of reactants to final products[16]. Generally, there are two types of catalysts; the homogeneous catalyst is a single atom, ion, or molecule and is in the same phase as the reactants. In other words, homogeneous catalyst particles can be dissolved in the reaction mixture easily. This catalyst is consumed in the reaction and produced. The advantages of this type of catalyst are very high activity, selectivity, and good efficiency. Improvements in the performance of homogeneous catalysts can be achieved by attaching different organic and inorganic groups to the parent particle. Despite the high efficiency of the homogeneous catalysts, the main problem with this type of catalyst is that after the reaction is complete, separating the dissolved catalyst from the final mixture is not easy. This problem is a significant challenge, especially when the catalyst is consumed in small amounts[17]. The second type of catalyst is the heterogeneous catalysts, which are in another phase with the reactants, unlike the homogeneous catalyst. For example, the reactants are in the liquid phase (in solution), but the catalyst is solid[18]. The size and properties of the heterogeneous catalyst particles are such that they do not dissolve easily in the reaction medium. Unlike homogeneous catalysts, heterogeneous catalysts are easily (with less cost, time, and materials) separated from the reaction mixture and do not cause product impurities. In order to compensate for the lack of active surface in such compounds, it is necessary to use a support in the role of the catalyst support[19]. The substrate is usually a porous structure with a high active surface. Industry uses heterogeneous processes more than homogeneous catalysts in the sight of the simple workup, ease of handling, and separations[20].

Researchers showed considerable interest in magnetic NPs (MNPs) in recent decades because of their special magnetic responsivity, facile recovery, biocompatibility, high magnetic susceptibility, low toxicity, and large surface area [21–23]. Heterogeneous catalysts are mostly utilized as nanoparticles regarding their larger available catalytic surface. One of the most useful procedures for preparing heterogeneous nanocatalysts is to immobilize complexes on solid bases like metal and metal oxides. Magnetic iron oxide nanoparticles (MNPs Fe_3O_4) have received a big deal of interest within metal oxide nanoparticles (NPs), probably because of their special applications[24–26]. Iron oxides have good magnetic properties compared to other magnetic nanoparticles and, on the other hand, show high stability against degradation[27,28]. By choosing a suitable synthesis method, the size, shape, surface coating, and colloidal stability of magnetic nanoparticles can be optimally controlled. Nowadays, the use of Fe_3O_4@SiO_2 core-shell composite nanoparticles has been developed as efficient catalysts for organic reactions[29–32]. They also can be used in various research fields such as data storage[33], gene manipulation[34,35], drug delivery[36–39], immunoassay[40,41], magnetic bio separation[42–44], magnetic resonance imaging (MRI)[45], environmental remediation[46–49], biomedicine[50–52], and catalysts[53–55].

Despite all related researches, the successful synthesis of a copper (II) complex through immobilizing the synthesized pyridine-4-carbaldehyde thiosemicarbazide ligand (L) on the magnetite nanoparticles coated

with silica (Fe_3O_4@SiO_2) surface and its use as a magnetic reusable catalyst for Cr (VI), MB, CR, and 4-NP reduction in the presence of $NaBH_4$ have not been reported. In this research, copper (II) complex was processed through immobilizing the synthesized pyridine-4-carbaldehyde thiosemicarbazide ligand (L) on the magnetite nanoparticles coated with silica (Fe_3O_4@SiO_2) surface as a novel, profitable, and magnetically reusable catalyst. Moreover, the catalytic performance of [Fe_3O_4@SiO_2-L-Cu(II)] was assessed for reducing Cr (VI), MB, CR, and 4-NP within an aqueous medium.

2. Experiments

2.1. Materials and Instruments

The chemical solvents and reagents used in this research have a high percentage of purity and were purchased from reputable companies Aldrich and Merck. The list of materials and solvents used is as follows: pyridine-4-carbaldehyde Sigma-Aldrich 97%, thiosemicarbazide 99%, Fe3O4 95%, TEOS ≥99%, (3-chloropropyl) trimethoxysilane 95%, K2CO3 ≥99%, CuCl2.2H2O ≥97%, 4-Nitrophenol ≥99%, Methylene blue, Congo Red, K2Cr2O7 ≥99%, HCOOH (88%), NaBH4 ≥98%, ethanol 98%, acetic acid ≥99%, NH3 ≥99%, dry toluene 99.8%, and DMF ≥99%. The Shimadzu 800IR 100FT-IR spectrometer was used to record the FT-IR spectra. The Hitachi U-2900 double-beam spectrophotometer with wavelengths in the 200-800 nm interval was used to obtain UV-Visible spectra. The TESCAN4992 device was used to perform an energy-dispersive X-ray (EDX) analysis. An accurate magnetometer of Iran Kavir VSMs was used to perform vibrating sample magnetometer measurements. Nanocatalyst's morphology was studied by applying FE-SEM images (ZEISS Sigma VP). STA 504 analyzer was applied in the argon atmosphere to perform thermal analysis (TG-DTG). Patterns of Powder XRD (XRD) obtained for the sample were examined utilizing a PANalytical X-PERT-PRO MPD diffractometer.

2.2. pyridine-4-carbaldehyde thiosemicarbazide ligand (L) preparation

In a 100 mL flask, we dissolved pyridine-4-carbaldehyde 97% (0.752 g) in ethanol 98%, followed by the addition of 1 drop of acetic acid. Then, it was mixed with thiosemicarbazide 99% (0.636 g) gradually. After adding the amine, the solution color turns yellow, indicating a Schiff base ligand. Afterward, the solution was stirred and refluxed for 12 h. Finally, we filtered the crystals and washed them with a small amount of cold ethanol (4°c). The L ligand is shown in Scheme 1.

2.3. [Fe_3O_4@SiO_2-L-Cu(II)] catalyst synthesis procedure

The following route was performed for synthesizing [Fe_3O_4@SiO_2-L-Cu(II)] complex. In the first step, 4.0 g of Fe_3O_4, 230.0 ml of EtOH, 10.0 ml of NH_3, 80.0 ml of H_2O, and 6.0 ml of tetraethylorthosilicate (TEOS) were strongly blended for 12 h in reflux circumstances and ultrasonicated for 30 min. In the next phase, 5.0 g of synthesized Fe_3O_4@SiO_2 was mixed with 3.0 mmol of (3-chloropropyl) trimethoxysilane and 300.0 ml of dry toluene and refluxed for 24 hours at 110°C. The precipitate obtained was assembled with an external magnetic field and rinsed with dry toluene and Deuterium-depleted water (DDW), followed by

oven-drying at 80°C for 6 h. Afterward, to synthesize the Fe_3O_4@SiO_2@$(CH_2)_3$-L, 2.0 g of the Fe_3O_4@SiO_2@(CH_2)3Cl, 0.9 g of the L (5.0 mmol), 50.0 mL of DMF, and 0.691 g of K_2CO_3 (5.0 mmol) were combined then refluxed for 24 hours. The resultant solid product was assembled via an external magnetic field, scoured by DMF, and parched. In the end, 1.0 g of the precipitate obtained to construct the Fe_3O_4@SiO_2-L-Cu(II) complex was introduced into 0.5 g of $CuCl_2.2H_2O$ and 50.0 mL of EtOH while stirring the earned reaction mixture vigorously in refluxing ethanol for 24 hours.

2.4. Catalytic reduction of 4-NP with applying [Fe_3O_4@SiO_2-L-Cu(II)] catalyst

To assess the catalytic activities, different measures of [Fe_3O_4@SiO_2-L-Cu(II)] (7.0,5.0,3.0 mg) were introduced to 4-NP aqueous solution (25 ml) (2.5 mM). Shortly after, 25 mL of the fresh sodium tetrahydroborate aqueous solution (0.25 M) was inserted, followed by stirring the mixture at ambient temperature (r.t). During the reaction, the absorbance of the solution was recorded by a UV-Vis spectrophotometer. The gradual disappearance of the soluble yellow color indicates that 4-AP has been obtained from 4-NP.

2.5. Catalytic degradation of CR and MB by employing [Fe_3O_4@SiO_2-L-Cu(II)] complex

In another work, two water-soluble organic dyes, Congo Red (CR) and Methylene blue (MB) were selected as a sample for the degradation applying [Fe_3O_4@SiO_2-L-Cu(II)] in the existence of reduction agent $NaBH_4$. Typically in a reduction process, 7.0 mg of the prepared catalyst was inserted into 25 mL of aqueous dye solution (3.1×10^{-5} M). Then, 25 ml fresh sodium tetrahydroborate solution (0.025M) was mixed with the product and blended at r.t. UV-Vis spectroscopy was used to make the reaction. At the end of the reaction, an external magnetic field was used to separate [Fe_3O_4@SiO_2-L-Cu(II)], followed by its rinsing by doubly distilled H_2O and reuse.

2.6. Catalytic reduction of Cr(VI) via [Fe_3O_4@SiO_2-L-Cu(II)] complex

The reductive ability of the catalyst was evaluated by reducing the Cr(VI) to Cr(III). Under constant stirring, 7.0 mg of [Fe_3O_4@SiO_2-L-Cu(II)] was inserted into 25 mL of 3.4×10^{-3} M $K_2Cr_2O_7$ solution and 1.0 mL HCOOH (88%) at 50°C. UV-Vis spectroscopy was used for monitoring the reduction process. When the reaction medium's yellow color disappeared, the nano-catalyst was effortlessly separated and re-utilized.

3. Results And Discussion

Studying L ligand

Enol-ketone tautomerization is a typical occurrence in many carbazone ligands. When tautomerization occurs, it results in binding hydrogen to sulfur on a nitrogen atom near to thiocarbonyl ligand. Thus, the ligand gains a negative charge. Scheme 2 indicates that the tautomerization may also occur in the L ligand. Subsequently, the ligand binds to the enolate form in the complex formation[56].

Table 1 presents the physical properties of the L ligand.

Table 1. physical properties of L ligand

compound	Molecular formula	Molar mass	color	Melting point	Yield (%)
L	$C_7H_8N_4S$	180 g/mol	cream	200	80 %

FT-IR spectroscopy was used for identifying the resulting ligands. The FT-IR spectrum of L ligand is shown in Fig. 1.

According to the FT-IR spectroscopy results, the band of the amine tensile vibration for the L ligand in the 3425.98 cm^{-1} region is a sharp band. The main band in the spectrum of Schiff base L ligands is from the imine functional group and the hydrogen on the nitrogen atom N^3 of the ligands. Since the imine-related band was observed, it demonstrates that a Schiff Base product has been formed. The band equivalent to the imine $v_{C=N}$ for the L ligand is a sharp band in the 1602.13 cm^{-1} region.

Because of the synthetic ligand structure and observing a hydrogen atom bonded to the nitrogen of the thiosemicarbazide, this ligand is expected to work as a neutral ligand by preserving this hydrogen or work as an anionic ligand by loss of this hydrogen. The related band v_{N-H} for the L ligand is a sharp band in the region of 3162.34 cm^{-1}. The peak correspondent to $v_{C=S}$ for the L ligand is in the 1703.36 cm^{-1} region. Because of the synthetic ligand structure, this ligand is expected to work as a di-dentate or a mono-dentate ligand. The coordination way of the synthetic Schiff base ligand to the metallic ion is shown in Scheme 3.

Characterizing the catalyst

The steps of the synthesis of [Fe_3O_4@SiO_2-L-Cu(II)] are presented in Scheme 4. EDS, FT-IR, VSM, TG-DTA, XRD, and FESEM analyses were used to characterize the prepared catalyst.

The FT-IR spectrum was performed to approve the coordination of the Cu atom by the L ligand and immobilizing the complex over the surface of Fe_3O_4@SiO_2 (Fig. 2). The Fe-O band's absorption peaks in the Fe_3O_4 MNPs appeared at around 623 cm^{-1}. The absorption peak at 458, 798, 1096 cm^{-1} are attributed to the Si-O bending, Si-O-Si stretching, and Si-O-Si bending in Fe3O4@SiO2. Furthermore, the absorption peaks at surrounding 3340 and 3390 cm^{-1} exhibits the N-H stretching modes of the L ligand of the Fe_3O_4 NPs. Also, the peak at 1626 is indexed to the C=N stretching band of L ligand, showing the grafting of the ligand over the Fe_3O_4@SiO_2 surface.

The [Fe_3O_4@SiO_2-L-Cu(II)] XRD patterns at 2θ are showed in Fig. 3. The appreciable peaks at 2θ = 41.25°, 50.7°, and 68.34° are associated to (111), (200), and (220) planes, respectively, suggesting the face-centered cubic crystalline structure of Cu NPs in a cubic face. The XRD spectrum of the [Fe_3O_4@SiO_2-L-Cu(II)] showed six intense peaks with 2θ amounts of 15.51°, 29.2°, 35.56°, 41.25°, 56.34°, and 62.91°,

which are attributed to the (110), (220), (311), (400), (511), and (440) faces of Fe_3O_4 nanoparticles, respectively.

The magnetic attributes of the complex of Fe_3O_4@SiO_2-L-Cu(II) were assessed at room temperature by vibration sample magnetometer (VSM) analysis (Fig. 4). The saturation magnetization (Ms) of the Fe_3O_4@SiO_2-L-Cu(II) complex is less than Fe_3O_4 MNPs. As shown in Fig. 4, by adding the complex and SiO_2 in the Fe_3O_4 MNPs surface, the saturation magnetization of the Fe_3O_4 core declined from around 60.0 emu g^{-1} to 21.0 emu g^{-1}.

EDS analysis was also performed to characterize chemical compositions of the [Fe_3O_4@SiO_2-L-Cu(II)] complex. As shown in Fig. 5, this analysis approved that [Fe_3O_4@SiO_2-L-Cu(II)] contained Fe, S, O, Cl, Si, and Cu and showed that Cu complex was coated on the Fe_3O_4@SiO_2 surface.

The surface morphology of the synthesized nanocatalyst was evaluated by using the field emission scanning microscopy (FE-SEM) analysis. According to FE-SEM assessments, the obtained nanoparticles are of various sizes, less than 100 nm, and have a spherical shape. Besides, as presented in Fig. 6, [Fe_3O_4@SiO_2-L-Cu(II)] possesses a core-shell structure.

The weight loss recognized at 100 ℃ is related to the deletion of organic solvents or water existent in the specimen; the weight loss from 200 to 300 ℃ is due to the consecutive cleavage of organic moieties, and the weight loss at 400-500 ℃ is due to the disintegration of L ligand and other organic groups. Eventually, exceeding 800 ℃, the weight loss is caused by the disintegration of the catalyst (Fig. 7).

The catalytic function of [Fe_3O_4@SiO_2-L-Cu(II)] was assessed by reducing 4-Nitrophenol to 4-Aminophenol in aqueous media in the existence of sodium tetrahydroborate. The reduction occurs only in the attendance of the catalyst, and the reduction does not occur when no [Fe_3O_4@SiO_2-L-Cu(II)] exists. Table 2 represents the reaction durations for the catalytic reduction of 4-Nitrophenol in the existence of $NaBH_4$ and various values of catalyst. According to the table, the reaction is completed faster by incrementing the amount of catalyst and $NaBH_4$. While there is no catalyst, the reduction protocol was not finished in 100 min. The ideal outcome was attained with 7.0 mg of [Fe_3O_4@SiO_2-L-Cu(II)] and 100 equivalents $NaBH_4$ (Table2, entry3).

Table 2. Optimal conditions for reducing the 4-NP applying [Fe_3O_4@SiO_2-L-Cu(II)] at r.t.

Entry	NaBH4 (equivalents)	Catalyst (mg)	Time
1	100	-	Not reaction
2	-	[Fe_3O_4@SiO_2-L-Cu(II)] (7.0)	Not reaction
3	**100**	**[Fe_3O_4@SiO_2-L-Cu(II)] (7.0)**	**114 s**
4	79	[Fe_3O_4@SiO_2-L-Cu(II)] (7.0)	135 s
5	50	[Fe_3O_4@SiO_2-L-Cu(II)] (7.0)	192 s
6	100	[Fe_3O_4@SiO_2-L-Cu(II)] (5.0)	125 s
7	79	[Fe_3O_4@SiO_2-L-Cu(II)] (5.0)	159 s
8	50	[Fe_3O_4@SiO_2-L-Cu(II)] (3.0)	182 s
9	100	[Fe_3O_4@SiO_2-L-Cu(II)] (3.0)	140 s

As presented in Scheme 5, the magnetic catalyst performs an influential role via the electron relay effects in the donor BH_4^- and acceptor nitro groups. The catalytic reduction of 4-Nitrophenol occurs in two stages: first, diffusion of BH_4^- and 4-NP from aqueous solution to the catalyst's surface through π-π stacking interactions, and second, the transfer of the electron mediated with the [Fe_3O_4@SiO_2-L-Cu(II)] surface from BH_4^- to 4-AP.

We used the UV-Vis spectrum to monitor the 4-Nitrophenol reduction to 4-Aminophenol protocol at r.t (Fig. 8). After the addition of the $NaBH_4$ solution to the catalyst and 4-NP mixture, the absorption peaks of 4-NP at 317 nm change to 400 nm, leading to the creation of 4-nitrophenolate ions. Furthermore, with a gradual decline and disappearance of the absorption peak at 400 nm with the [Fe_3O_4@SiO_2-L-Cu(II)], a new peak emerged at around 297 nm, indicating that 4-Aminophenol was obtained from 4-Nitrophenol.

3.3. Cr(VI) catalytic reduction utilizing [Fe_3O_4@SiO_2-L-Cu(II)]

As Cr(VI) is very dangerous to live organisms, it should be quickly removed before discharging into the environment. Similar to the above reports, the catalytic behavior of [Fe_3O_4@SiO_2-L-Cu(II)] in reducing Cr(VI) to Cr(III) was investigated utilizing the HCOOH aqueous solution. The Cr(VI) was reduced via transferring hydrogen from HCOOH as an electron transfer from ligand (O) to Cr(VI) and a hydrogen donor to metal (Cr(VI)) (Scheme 6). Without generating the intermediated compounds, the HCO_2H is decomposed onto Cu(II) surface, and CO_2 and H_2 form as a suitable product.

We used UV-Vis absorption spectroscopy to monitor the reduction of Cr(VI) protocol, which indicates a feature absorption peak of 350 nm (Figure 9). Figure 9 illustrates the reduction of the chromium(VI) aqueous solution that occurred by existing [Fe_3O_4@SiO_2-L-Cu(II)] and HCO_2H at various time intervals. The experimental results were epitomized and presented in Table 2. When there is no catalyst, the HCO_2H-mediated transfer of Cr(VI) did not decline after 100 min (Table 3, entry 1). By adding [Fe_3O_4@SiO_2-L-Cu(II)], the HCO_2H-mediated reduction of chromium(VI) declines with changing color from yellow to no color, as well as the invisibility of the absorption band at 350 nm during 50 s. The ideal outcome was yielded with 7.0 mg of [Fe_3O_4@SiO_2-L-Cu(II)] and 1.0 ml of the aqueous HCO_2H solution (Table 3, entry2).

Table 3. Optimizing conditions for the Cr(VI) degradation applying [Fe_3O_4@SiO_2-L-Cu(II)] and HCOOH at 50°C

Entry	Formic acid	Catalyst (mg)	Time
1	1.0 mL	-	No reaction
2	**1.0 mL**	**[Fe_3O_4@SiO_2-L-Cu(II)] (7.0)**	**11 min**
3	1.0 mL	[Fe_3O_4@SiO_2-L-Cu(II)] (5.0)	19 min
4	1.0 mL	[Fe_3O_4@SiO_2-L-Cu(II)] (3.0)	29 min

3.4. Catalytic degradation of CR and MB by utilizing and [Fe_3O_4@SiO_2-L-Cu(II)]

We assessed the catalytic efficiency of [Fe_3O_4@SiO_2-L-Cu(II)] toward degrading the CR and MB with the maximum absorption at 498 nm and 663 nm, respectively. UV-Vis absorption spectroscopy was used for monitoring the reduction procedure (Figs. 10 and 11). The degradation of CR and MB was completed without any delay in the existence of [Fe_3O_4@SiO_2-L-Cu(II)]. Table 4 represents the results of degradation MB and CR.

Table 4. Optimizing conditions for the degradation of the Congo Red and Methylene Blue applying [Fe_3O_4@SiO_2-L-Cu(II)]

Entry	Dye	Catalyst (mg)	$NaBH_4$ (M)	Time
1	**MB**	**[Fe_3O_4@SiO_2-L-Cu(II)] (7.0)**	**5.3×10^{-3}**	**Immediately**
2	MB	[Fe_3O_4@SiO_2-L-Cu(II)] (5.0)	5.3×10^{-3}	3 s
3	**CR**	**[Fe_3O_4@SiO_2-L-Cu(II)] (7.0)**	**5.3×10^{-3}**	**Immediately**
4	CR	[Fe_3O_4@SiO_2-L-Cu(II)] (5.0)	5.3×10^{-3}	6 s
5	CR	[Fe_3O_4@SiO_2-L-Cu(II)] (3.0)	5.3×10^{-3}	15 s

4. Catalyst Reusability

Synthesizing recyclable nanocatalysts with high catalytic performance is an essential issue from green and environmental viewpoints. The reusability of the magnetic nanocomplex [Fe_3O_4@SiO_2-L-Cu(II)] in the reduction reaction of 4-Nitrophenol was evaluated in this study. As displayed in Fig. 12, [Fe_3O_4@SiO_2-L-Cu(II)] nanocomplex catalyzed the 4-NP reduction several times. By ending the reduction reaction, an external magnetic field was considered for isolating the catalyst and reused in the successive run without remarkable loss of catalytic efficiency. The gradual deactivation of [Fe_3O_4@SiO_2-L-Cu(II)] approves the high constancy of the catalyst under the reaction condition.

5. Conclusions

This research aims to provide a facile and convenient manner for immobilizing the organic copper complex on the surface of Fe_3O_4@SiO_2 as a magnetic heterogeneous and reusable nanocatalyst for the degradation/reduction of 4-NP, Cr(VI), MB, and CR in the medium conditions. The methods for characterizing the [Fe_3O_4@SiO_2-L-Cu(II)] were SEM, VSM, FT-IR, XRD, TG-DTA, and EDS. We found that this catalyst is efficient for the reduction/degradation of environmental pollutants in an aqueous medium, and this method has good advantages such as higher performance, reduction of environmental risks, and a very convenient working method.

Declarations

Acknowledgments

Here, the Research Council of the Qom University is thanked for the partial supports.

References

1. M. Ismail, K. Akhtar, M. I. Khan, T. Kamal, M. A. Khan, A. M. Asiri, J. Seo, and S. B. Khan, Current Pharmaceutical Design **25**, 3645 (2019).

2. D. Prabakar, S. Suvetha K, V. T. Manimudi, T. Mathimani, G. Kumar, E. R. Rene, and A. Pugazhendhi, Journal of Environmental Management **218**, 165 (2018).

3. G. Selvi, M. Tercan, N. Özdemir, and O. Dayan, Applied Organometallic Chemistry **34**, e6009 (2020).

4. A. Bagherzade, F. Nemati, H. T. Nahzomi, and A. Elhampour, Journal of Molecular Structure **1185**, 38 (2019).

5. S. Farhadi and F. Siadatnasab, Journal of Molecular Structure **1123**, 171 (2016).

6. K. Singh and S. Arora, Critical Reviews in Environmental Science and Technology **41**, 807 (2011).

7. A. Serrà, R. Artal, M. Pozo, J. Garcia-Amorós, and E. Gómez, Catalysts **10**, 458 (2020).

8. M. A. Subhan, S. S. Jhuma, P. Chandra Saha, M. M. Alam, A. M. Asiri, M. Al-Mamun, S. A. Attia, T. H. Emon, A. K. Azad, and M. M. Rahman, New Journal of Chemistry **43**, 10352 (2019).

9. M. Nameni, M. R. Alavi Moghadam, and M. Arami, International Journal of Environmental Science & Technology **5**, 161 (2008).

10. S. Mitra, A. Sarkar, and S. Sen, Nanotechnology for Environmental Engineering **2**, (2017).

11. Y. Wang, H. Su, Y. Gu, X. Song, and J. Zhao, OncoTargets and Therapy **10**, 4065 (2017).

12. D. G. Barceloux and D. Barceloux, Journal of Toxicology: Clinical Toxicology **37**, 173 (1999).

13. R. R. Ray, Interdisciplinary Toxicology **9**, 55 (2016).

14. L. B. Khalil, W. E. Mourad, and M. W. Rophael, Applied Catalysis B: Environmental **17**, 267 (1998).

15. S. Chakrabarti, B. Chaudhuri, S. Bhattacharjee, A. K. Ray, and B. K. Dutta, Chemical Engineering Journal **153**, 86 (2009).

16. Q. Zhang, X. Yang, and J. Guan, ACS Applied Nano Materials **2**, 4681 (2019).

17. S. Albonetti, R. Mazzoni, and F. Cavani, *Homogeneous, Heterogeneous and Nanocatalysis* (2015).

18. R. Schlögl, Angewandte Chemie - International Edition **54**, 3465 (2015).

19. A. Corma and H. Garcia, Topics in Catalysis **48**, 8 (2008).

20. H. H. Mardhiah, H. C. Ong, H. H. Masjuki, S. Lim, and H. V. Lee, Renewable and Sustainable Energy Reviews **67**, 1225 (2017).

21. L. H. Reddy, J. L. Arias, J. Nicolas, and P. Couvreur, Chemical Reviews **112**, 5818 (2012).

22. R. Mehdaoui, S. Agren, A. Dhahri, J. El Haskouri, E. Beyou, M. Lahcini, and M. H. V. Baouab, Applied Organometallic Chemistry e6257 (2021).

23. G. Kibar and A. Tuncel, Journal of Inorganic and Organometallic Polymers and Materials **28**, 2249 (2018).

24. X. H. Pham, E. Hahm, H. M. Kim, B. S. Son, A. Jo, J. An, T. A. T. Thi, D. Q. Nguyen, and B. H. Jun, Nanomaterials **10**, (2020).

25. M. Nasrollahzadeh, Z. Issaabadi, H. Ali Khonakdar, and U. Wagenknecht, Separation and Purification Technology **203**, 185 (2018).

26. D. Habibi, S. Heydari, A. Gil, M. Afsharfarnia, A. Faraji, R. Karamian, and M. Asadbegy, Applied Organometallic Chemistry **32**, e4005 (2018).

27. P. Mohammadi and H. Sheibani, Applied Organometallic Chemistry **32**, e4249 (2018).

28. E. Kalantari, M. A. Khalilzadeh, and D. Zareyee, Journal of Inorganic and Organometallic Polymers and Materials **31**, 319 (2021).

29. E. Kalantari, M. A. Khalilzadeh, D. Zareyee, and M. Shokouhimehr, Journal of Molecular Structure **1218**, 128488 (2020).

30. A. H. Kianfar and M. A. Arayesh, Journal of Environmental Chemical Engineering **8**, 103640 (2020).

31. Z. M. Shammi, A. H. Kianfar, and M. M. Momeni, Journal of Materials Science: Materials in Electronics **31**, 14810 (2020).

32. F. Ghasemy-Piranloo, S. Dadashian, and F. Bavarsiha, Journal of Inorganic and Organometallic Polymers and Materials **30**, 3740 (2020).

33. B. Shen and S. Sun, Chemistry - A European Journal **26**, 6757 (2020).

34. S. C. McBain, H. H. P. Yiu, and J. Dobson, International Journal of Nanomedicine **3**, 169 (2008).

35. M. Subramanian, A. Miaskowski, S. I. Jenkins, J. Lim, and J. Dobson, Applied Physics A: Materials Science and Processing **125**, 1 (2019).

36. N. Knežević, I. Gadjanski, and J. O. Durand, Journal of Materials Chemistry B **7**, 9 (2019).

37. S. Mirza, M. S. Ahmad, M. I. A. Shah, and M. Ateeq, *Magnetic Nanoparticles: Drug Delivery and Bioimaging Applications* (Elsevier Inc., 2019).

38. A. Gholami, S. M. Mousavi, S. A. Hashemi, Y. Ghasemi, W. H. Chiang, and N. Parvin, Drug Metabolism Reviews **52**, 205 (2020).

39. L. Shen, B. Li, and Y. Qiao, Materials **11**, (2018).

40. D. M. Bruls, T. H. Evers, J. A. H. Kahlman, P. J. W. Van Lankvelt, M. Ovsyanko, E. G. M. Pelssers, J. J. H. B. Schleipen, F. K. De Theije, C. A. Verschuren, T. Van Der Wijk, J. B. A. Van Zon, W. U. Dittmer, A. H. J. Immink, J. H. Nieuwenhuis, and M. W. J. Prins, Lab on a Chip **9**, 3504 (2009).

41. B. Star, Supplementary Infomation **22**, 0 (2013).

42. H. Fatima and K. S. Kim, Korean Journal of Chemical Engineering **34**, 589 (2017).

43. D. W. Lee, H. Fatima, and K. S. Kim, Journal of Nanoscience and Nanotechnology **18**, 1414 (2018).

44. Q. Yang, Y. Dong, Y. Qiu, X. Yang, H. Cao, and Y. Wu, Colloids and Surfaces B: Biointerfaces **191**, 111014 (2020).

45. R. A. Revia and M. Zhang, Materials Today **19**, 157 (2016).

46. E. Pourian, S. Javanshir, Z. Dolatkhah, S. Molaei, and A. Maleki, ACS Omega **3**, 5012 (2018).

47. H. Mohammad Zaheri, S. Javanshir, B. Hemmati, Z. Dolatkhah, and M. Fardpour, Chemistry Central Journal **12**, 1 (2018).

48. M. Banazadeh, S. Amirnejat, and S. Javanshir, Frontiers in Chemistry **8**, 1 (2020).

49. U. Kurtan, A. Baykal, and H. Sözeri, Journal of Inorganic and Organometallic Polymers and Materials **25**, 921 (2015).

50. B. Cui, H. Peng, H. Xia, X. Guo, and H. Guo, Separation and Purification Technology **103**, 251 (2013).

51. C. Shasha and K. M. Krishnan, Advanced Materials **1904131**, 48 (2020).

52. R. V. Mehta, Materials Science and Engineering C **79**, 901 (2017).

53. R. Abu-Reziq, H. Alper, D. Wang, and M. L. Post, Journal of the American Chemical Society **128**, 5279 (2006).

54. A. R. Hajipour and P. Abolfathi, Catalysis Communications **103**, 92 (2018).

55. E. Abbasi Asl, M. Haghighi, and A. Talati, Separation and Purification Technology **251**, 117003 (2020).

56. Y. Hanifehpour, J. Dadashi, M. Khaleghian, M. Rezaei, B. Mirtamizdoust, S. Woo Joo, and R. Article, (2021).

Figures

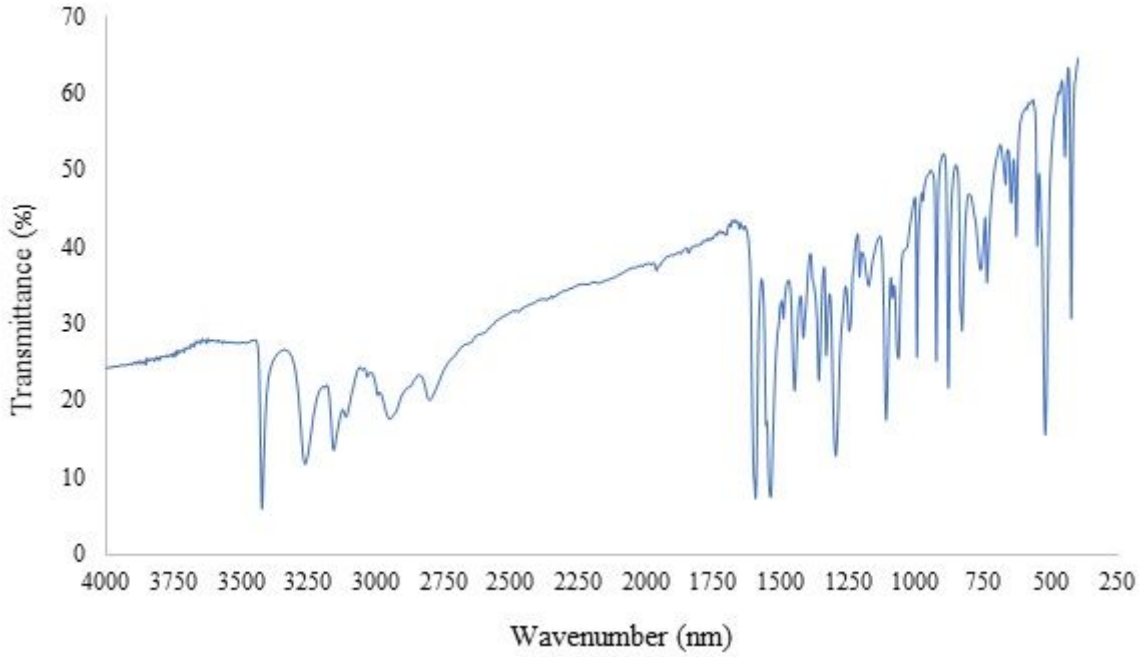

Figure 1

FT-IR spectrum of L ligand.

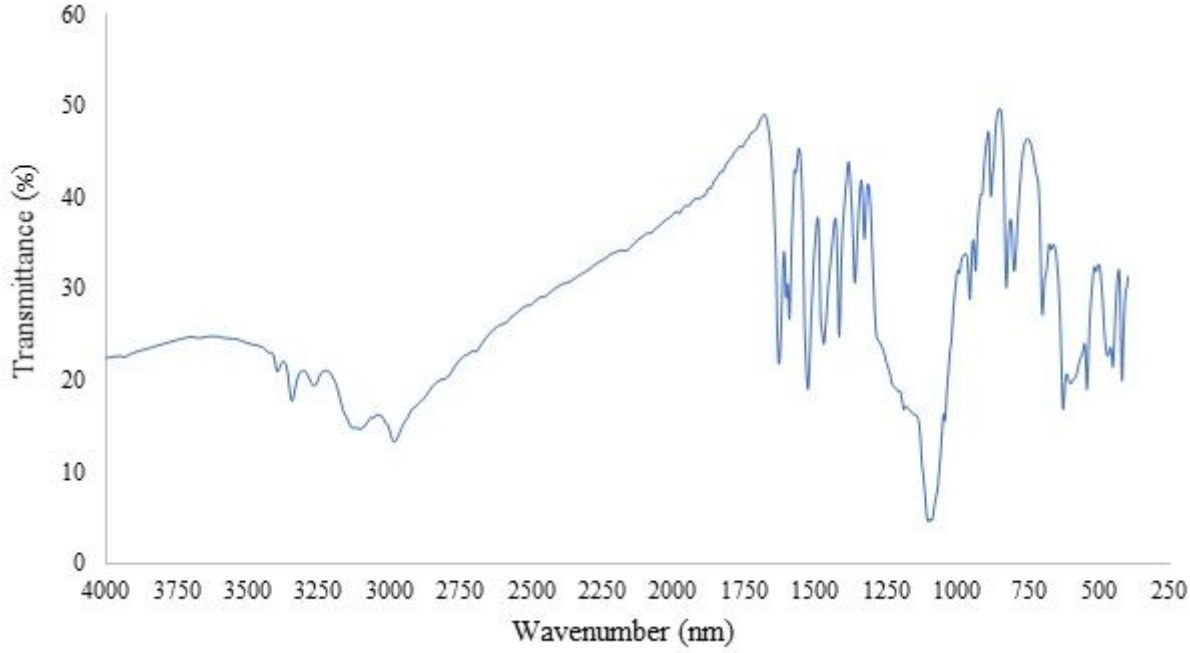

Figure 2

The FT-IR spectra of the [Fe3O4@SiO2-L-Cu(II)] complex.

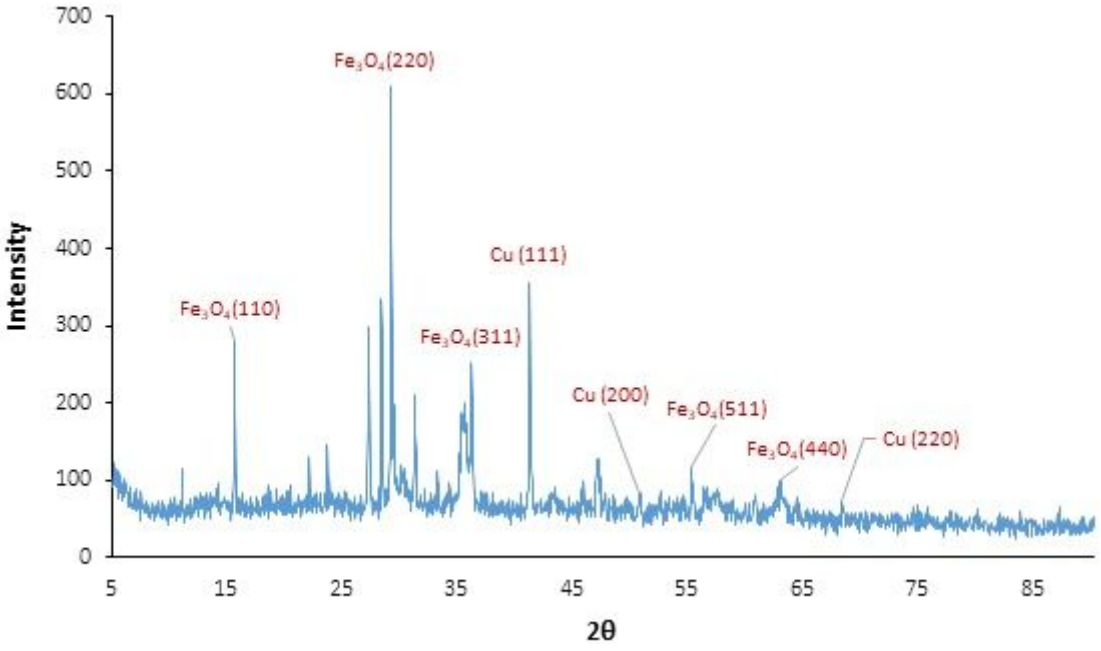

Figure 3

XRD pattern of [Fe3O4@SiO2-L-Cu(II)]

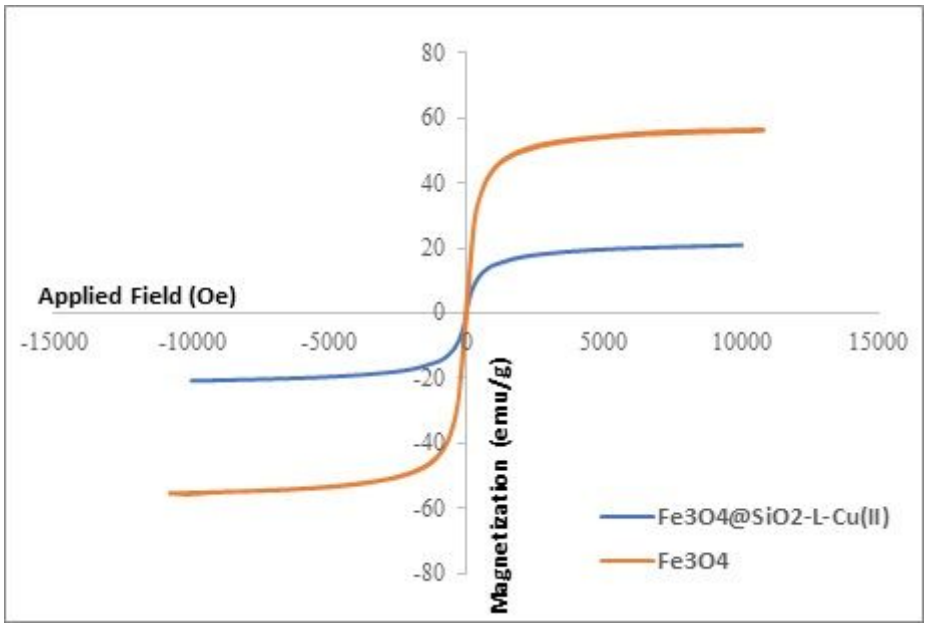

Figure 4

The magnetization curve for the magnetic nanocatalyst

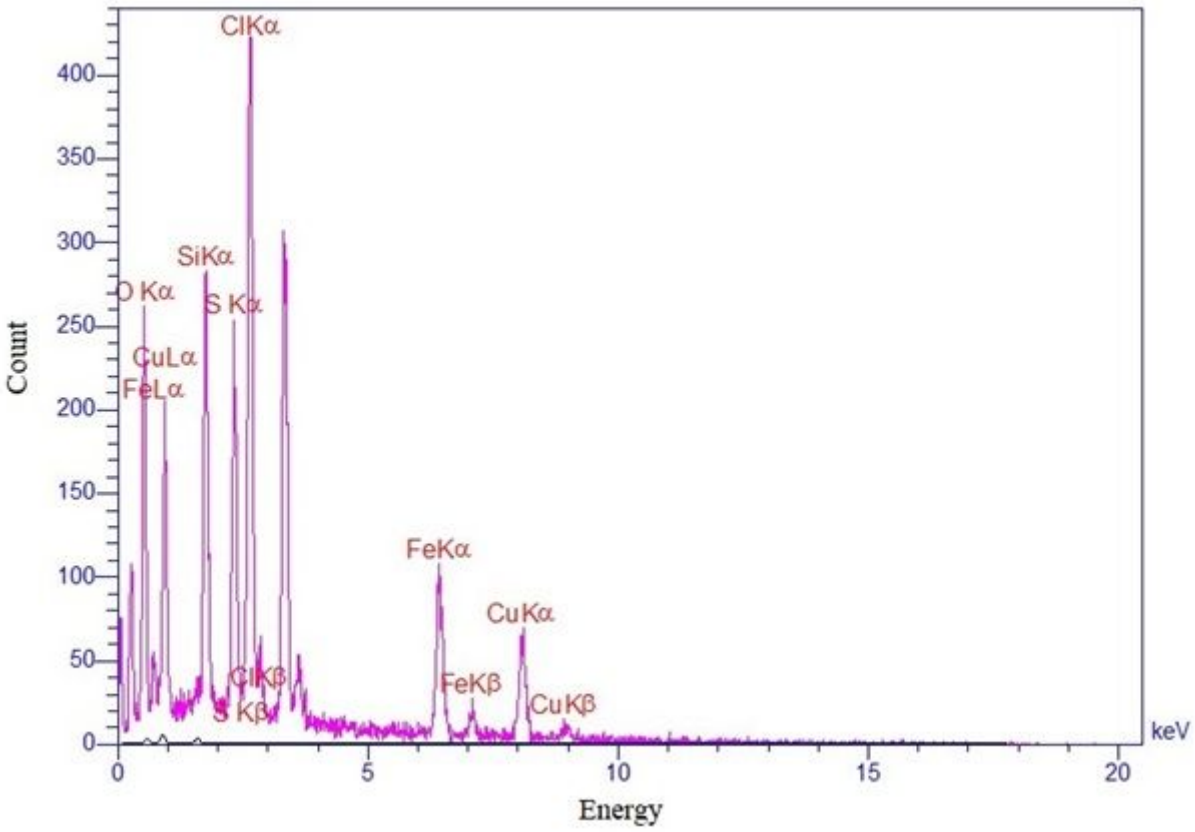

Figure 5

Energy dispersive x-ray spectrum of the [Fe3O4@SiO2-L-Cu(II)]

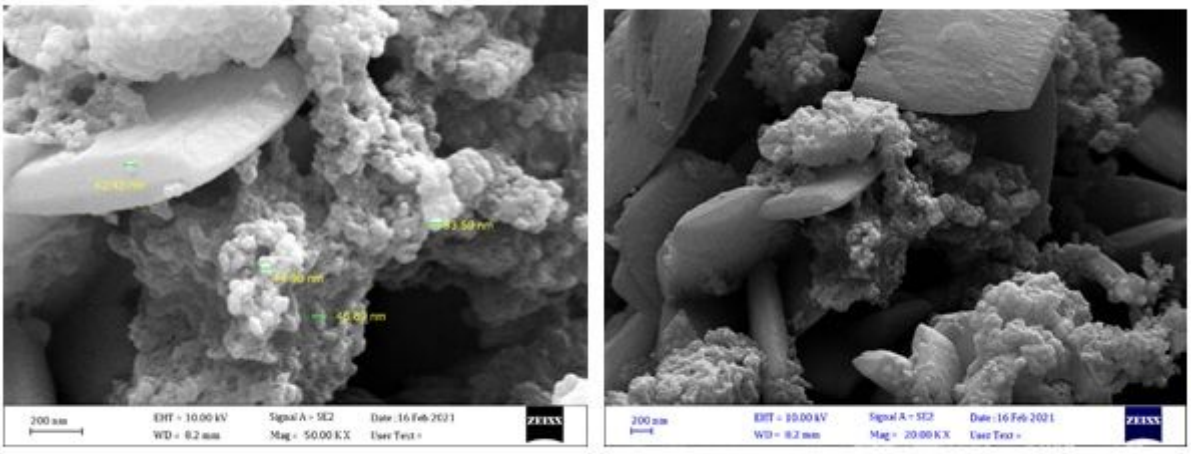

Figure 6

FE-SEM images of the [Fe3O4@SiO2-L-Cu(II)]

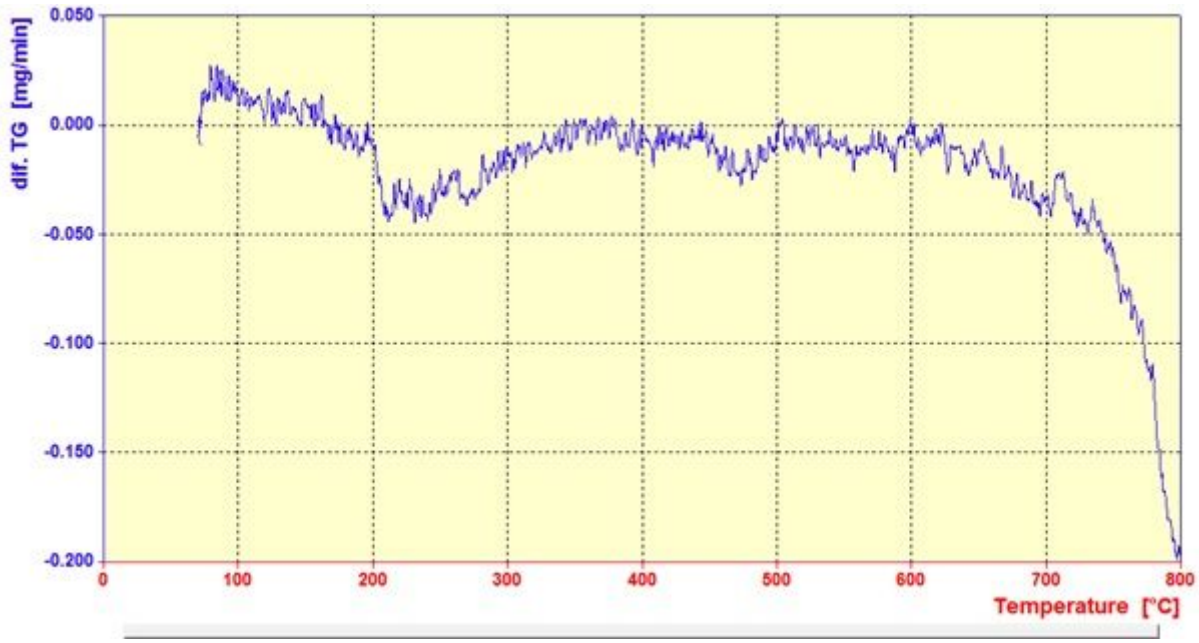

Figure 7

The thermogravimetric-differential thermal analysis data determined for the magnetic nanocatalyst

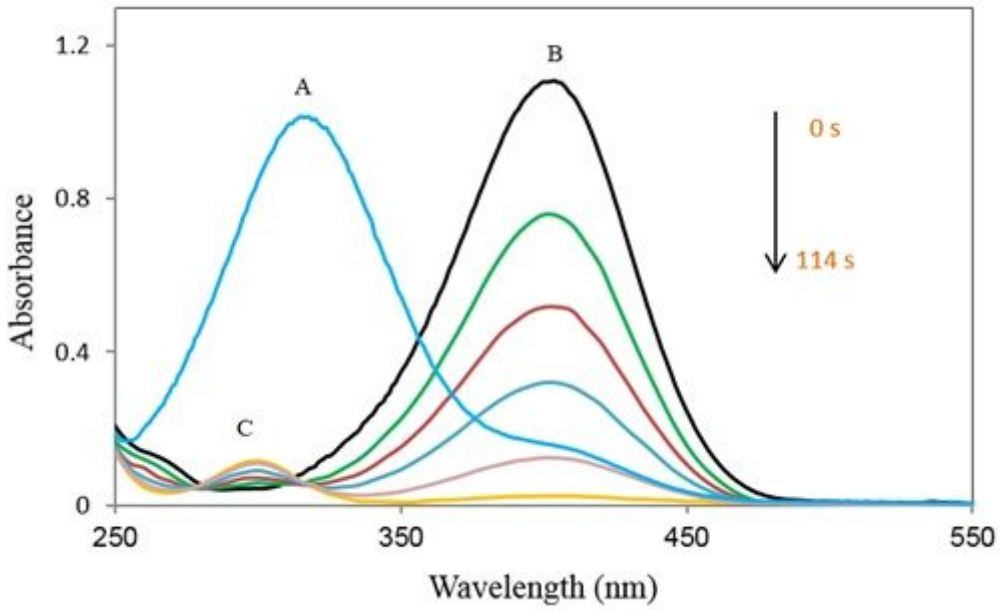

Figure 8

The UV-Visible spectrum of the 4-Nitrophenol reduced with NaBH4 in [Fe3O4@SiO2-L-Cu(II)]. A: 4-NP, B: 4-Nitrophenolate ion, C:4-AP

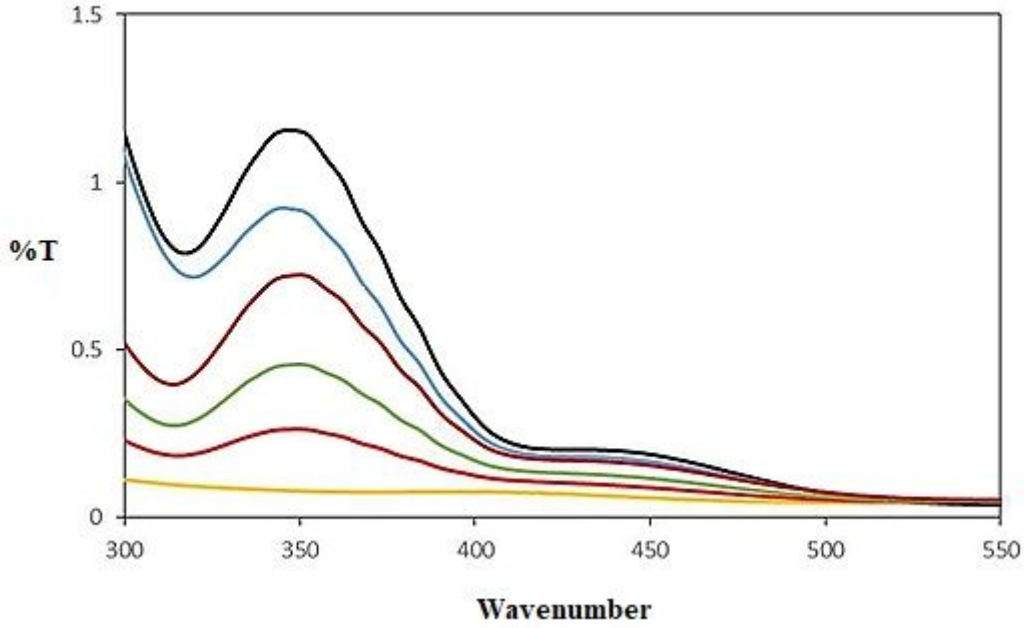

Figure 9

The Cr(VI) aqueous solution's UV-Vis spectra utilizing HCOOH (1.0 mL) and [Fe3O4@SiO2-L-Cu(II)]

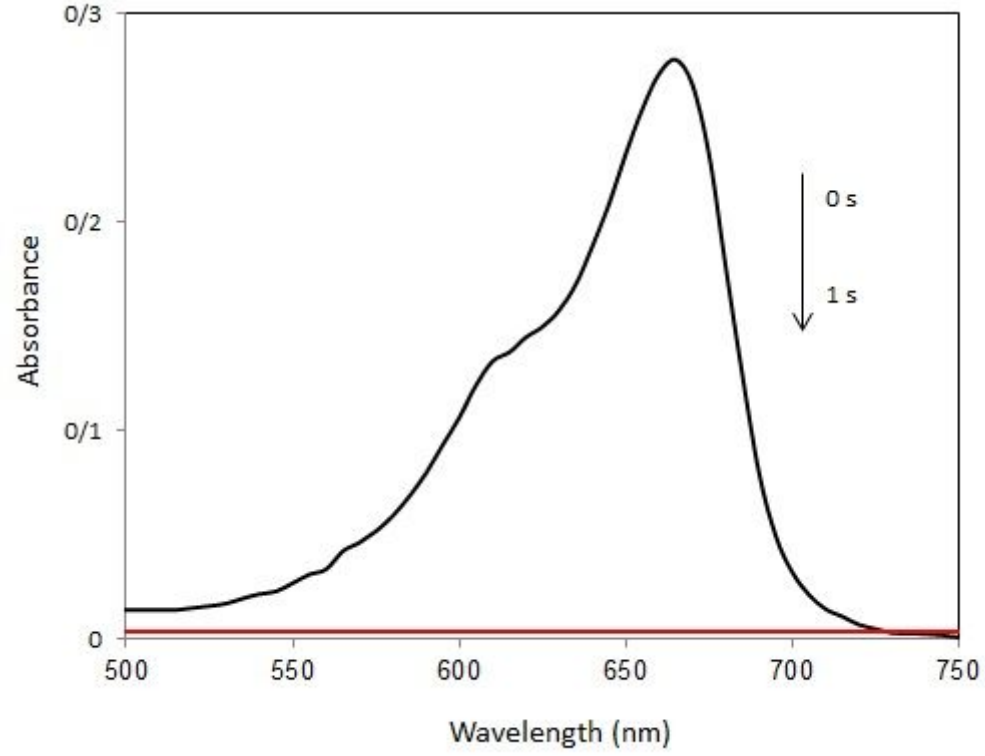

Figure 10

The UV-Visible spectrum of the Methylene Blue degraded by NaBH4 in [Fe3O4@SiO2-L-Cu(II)].

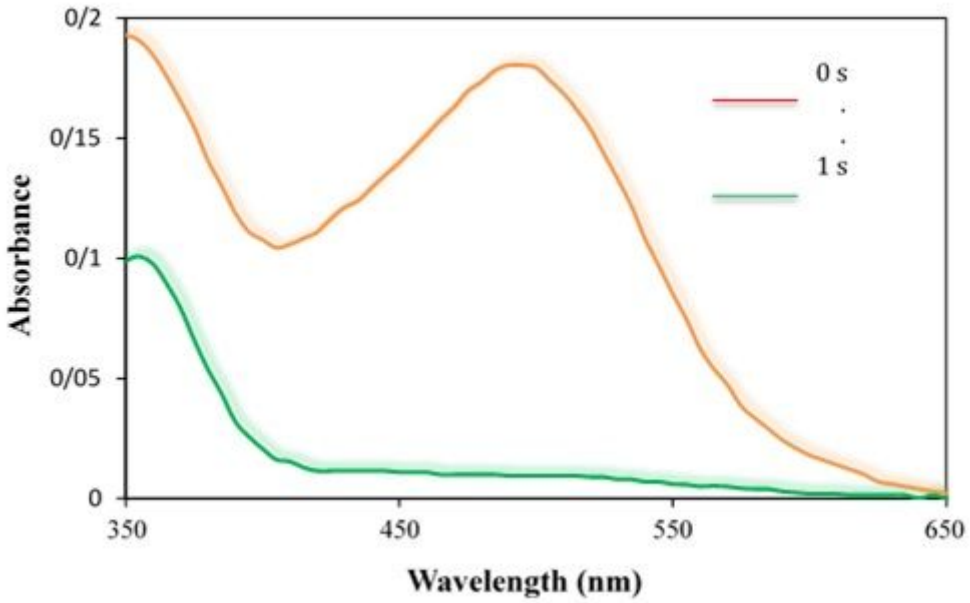

Figure 11

The UV-Visible spectrum of the degraded Congo Red by NaBH4 in [Fe3O4@SiO2-L-Cu(II)].

Figure 12

Magnetic removal and recoverability of nanocatalyst for 4-NP reduction at room temperature.

Supplementary Files

This is a list of supplementary files associated with this preprint. Click to download.

- Schemes.pdf